Solar Physics (2005) 225: 157–175

NUMERICAL MAGNETOHYDRODYNAMIC EXPERIMENTS FOR TESTING THE PHYSICAL MECHANISMS OF CORONAL MASS EJECTIONS ACCELERATION

S. T. WU[1,2], T. X. ZHANG[1], E. TANDBERG-HANSSEN[1], YANG LIU[3], XUESHANG FENG[4] and ARJUN TAN[5]

[1]*Center for Space Plasma and Aeronomic Research, University of Alabama in Huntsville, Huntsville, AL 35899, U.S.A.*

[2]*Department of Mechanical and Aerospace Engineering, University of Alabama in Huntsville, Huntsville, AL 35899, U.S.A.*

[3]*W. W. Hansen Experimental Physics Laboratory, Stanford University, Stanford, CA 94305-4085, U.S.A.*

[4]*Laboratory for Space Weather, Center for Space Science and Applied Research, Chinese Academy of Sciences, Beijing, 100080, P.R. China*

[5]*Department of Physics, Alabama A & M University, Normal, AL 35762, U.S.A.*

(Received 25 June 2004; accepted 27 July 2004)

Abstract. Analysis of observations from both space-borne (LASCO/SOHO, *Skylab* and Solar Maximum Mission) and ground-based (Mauna Loa Observatory) instruments show that there are two types of coronal mass ejections (CMEs), fast CMEs and slow CMEs. Fast CMEs start with a high initial speed, which remains more or less constant, while slow CMEs start with a low initial speed, but show a gradual acceleration. To explain the difference between the two types of CMEs, Low and Zhang (2002) proposed that it resulted from a difference in the initial topology of the magnetic fields associated with the underlying quiescent prominences, i.e., a normal prominence configuration will lead to a fast CME, while an inverse quiescent prominence results in a slow CME. In this paper we explore a different scenario to explain the existence of fast and slow CMEs. Postulating only an inverse topology for the quiescent prominences, we show that fast and slow CMEs result from different physical processes responsible for the destabilization of the coronal magnetic field and for the initiation and launching of the CME. We use a 2.5-D, time-dependent streamer and flux-rope magnetohydrodynamic (MHD) model (Wu and Guo, 1997) and investigate three initiation processes, viz. (1) injecting of magnetic flux into the flux-rope, thereby causing an additional Lorentz force that will destabilize the streamer and launch a CME (Wu *et al*., 1997, 1999); (2) draining of plasma from the flux-rope and triggering a magnetic buoyancy force that causes the flux-rope to lift and launch a CME; and (3) introducing additional heating into the flux-rope, thereby simulating an active-region flux-rope accompanied by a flare to launch a CME. We present 12 numerical tests using these three driving mechanisms either alone or in various combinations. The results show that both fast and slow CMEs can be obtained from an inverse prominence configuration subjected to one or more of these three different initiation processes.

1. Introduction

Since the discovery of coronal mass ejections (CMEs), some 30 years ago (Tousey, 1973), a wealth of data from both space borne (*Skylab*, Solar Maximum Mission, Solar and Heliospheric Observatory) as well as ground-based (Mauna Loa

Observatory) coronagraphs have enabled us to discover important kinematic characteristics of CMEs from 1.1 to ∼30 solar radii. These data reveal that all observed CMEs show one of the two distinct speed–height profiles (Gosling *et al*., 1976; MacQueen and Fisher, 1983; Sheeley *et al*., 1999; St. Cyr *et al*., 1999; Andrews and Howard, 2001). CMEs that originate from an active region accompanied by a flare usually have an initial speed well above the CME median speed, 400 km s^{-1} and are called fast CMEs, or constant speed CMEs. They show no significant acceleration, but may show some deceleration (St. Cyr *et al*., 2000). On the other hand, CMEs that originate above a quiescent prominence, away from active regions, have an initial speed much less than the medium speed and are referred to as slow CMEs. However, they show a gradual acceleration and may attain high speeds; they are referred to as accelerated CMEs.

It is well known that CMEs are closely related to the eruption of prominences, but the physical processes responsible for the two types of CMEs, i.e., for the two types of CME acceleration processes, have only recently been addressed. Low and Zhang (2002) proposed a model based on the observed two different types of magnetic topology found in quiescent prominences, viz. the normal and inverse configuration (Tandberg-Hanssen, 1995). The prominence material is levitated and held above the photospheric magnetic field by the prominence's own magnetic field, which runs along the neutral line that crosses the prominence, being anchored in the photosphere on either side of the prominence. A normal prominence configuration is distinguished by a magnetic field that threads across the prominence in the same direction as the photospheric magnetic field below. In an inverse prominence the two fields run in opposite directions.

Low and Zhang suggested that a fast CME will occur above a normal prominence and that a slow CME will occur above an inverse prominence. The physical reason for the difference is to be found in the different roles played by magnetic reconnection in the two cases. In the normal prominence case, the field lines in the leading edge of the prominence flux-rope are opposite to the field lines confined by the flux-rope; thus, a current sheet is formed, and magnetic reconnection occurs due to a tearing-mode instability. The magnetic reconnection will cause the field lines confined by the flux-rope to open, thereby removing flux ahead of the flux-rope, and cause it to escape outward. This explosive situation is similar to the "breakout" CME model proposed by Antiochos, DeVore, and Klumchuk (1999).

In the case of an inverse prominence, the expulsion of the flux-rope will cause a current sheet to form in the anchored bipolar photospheric field below the flux-rope (Amari *et al*., 2000). Since the currents of this configuration have the same direction as those in the flux-rope, they will attract each other and prevent the outward motion of the flux-rope. However, magnetic reconnection will cause the currents to dissipate, thereby slowly removing the attracting force. Since the magnetic reconnection does not directly affect the expulsion of the flux-rope, its outward motion is not explosive, and leads to a slow CME. This scenario is supported by recent observations (Zhang *et al*., 2002).

Liu *et al*. (2003) have performed a numerical simulation, using a two-dimensional, time-dependent streamer and flux-rope resistive magnetohydrodynamic (MHD) model (Guo *et al*., 1996), and their results agree well with Low and Zhang's scenario. On the other hand, Chen *et al*. (1997) and Wu *et al*. (1997) had studied the eruptive flux-rope in relation to LASCO CME. Recently, Chen and Krall (2003) have presented a single three-dimensional flux-rope model also to investigate the CME acceleration. This model is based on the Lorentz force as the only driving mechanism.

In the present study, we present a numerical experiment, using only the inverse prominence magnetic field topology, but specifying three different CME initiation processes, to investigate whether both fast and slow CMEs may result. Mathematically, the three different initiation processes are considered to be perturbed conditions at the lower boundary. They are as follows: (1) injection of magnetic flux into the flux-rope, thereby causing an additional Lorentz force that will destabilize the streamer and launch a CME (Wu *et al*., 1997, 1999); (2) draining of plasma from the flux-rope, and triggering a magnetic buoyancy force that causes the flux-rope to lift and launch a CME; and (3) introducing additional heating into the flux-rope, simulating an active-region flux-rope accompanied by a flare to launch a CME. The results show that the CME acceleration is closely related to one of these three processes, or to a combination thereof. In Section 2 we describe the model and the three initiation processes. Section 3 presents numerical results, and concluding remarks are given in Section 4.

2. Description of the Simulation Model

To perform the numerical experiment, the streamer and flux-rope model given by Wu and Guo (1997) is used. This model has successfully simulated some important features of several loop-like CMEs observed by the SOHO spacecraft coronagraph, LASCO (Wu, Guo, and Dryer, 1997; Wu *et al*., 1999, 2000; Plunkett *et al*., 2000). The mathematical representation of the model was discussed in detail by Wu and Guo (1997) and Wu *et al*. (1997). The governing equations are a set of single-fluid time-dependent, 2.5-D MHD equations which describe the conservation of mass, momentum, and ideal energy (without dissipation) together with the magnetic induction equation to account for the nonlinear interactions between the plasma flow and the magnetic field. These equations are identical to those given by Wu *et al*. (1997), and will not be repeated here. Physically, the streamer and the flux-rope model consist of two systems oriented orthogonally to each other as originally suggested by Low (1990). One system represents a helmet streamer and the other the flux-rope. The initial equilibrium configuration is constructed in two steps: (1) Prescribe a dipole magnetic field together with Parker's radial expanding solar wind as the input to the set of governing equations via a relaxation technique to obtain an equilibrium solution. This steady-state solution represents a coronal streamer

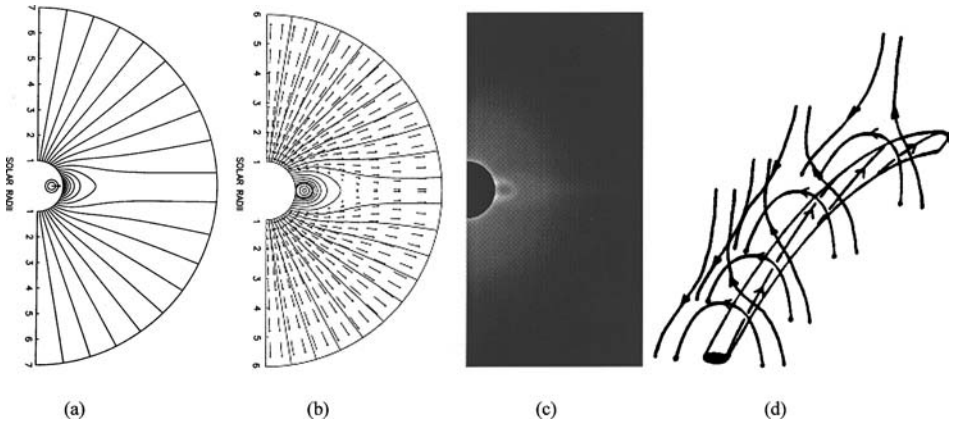

Figure 1. Simulated initial dynamical equilibrium state for a streamer and flux-rope system, (a) magnetic configuration of the streamer and the emerged flux-rope, (b) the dynamical equilibrium state of the magnetic field lines and velocity vectors of the streamer, the new-fully-emerged flux-rope and solar wind, (c) the polarization brightness of streamer and flux-rope structure, and (d) the schematic description of the system.

(Figure 1a) that is merged with a flux rope (i.e., the prominence) which is approximated by an axisymmetric magnetic toroidal solution (Shafranov, 1960). (2) The torodial flux-rope is numerically injected into the streamer from the lower boundary, again using the relaxation technique to obtain another equilibrium state (Figure 1b). Figure 1c shows the polarization brightness, and Figure 1d is a schematic representation of this streamer and flux-rope system. This configuration forms our initial state for the present numerical study of the CME acceleration. The physical parameters and each mode of energy and the total energy of this initial state are given in Tables I and II.

The computational domain is from $1R_s$ to $32R_s$ in the radial direction, where R_s is the solar radius, and from the north pole to the south pole in the meridional plane. Because the symmetry condition is chosen at the equator, the actual computation is from $-1^\circ \leq \theta \leq 91^\circ$. We used 202×92 grids, uniform in the meridional direction ($\Delta\theta = 1^\circ$). In order to better resolve the shock in the radial direction, the code has been modified to adopt a non-uniform grid in the r-direction ($\Delta r_i = r_i - r_{i-1} = 0.0175 r_{i-1}$). This gives a better resolution near the solar surface, and resolves the shock development due to acceleration. Note that the presentation in the paper is displayed from the north pole ($\theta = 0^\circ$) to the south pole ($\theta = 180^\circ$), by simply mirroring the computational domain symmetrically above the equator.

The numerical scheme used to solve this set of MHD equations is the combined difference technique described by Wu, Guo, and Wang (1995), Wu *et al.* (1997, 1999). The boundary conditions are based on the method of projected characteristics (Wu and Wang, 1987) at the lower boundary. These lower boundary conditions are updated as time progresses. At the pole and equator, symmetrical conditions are used. All the properties at the outer boundary employ the linear extrapolation

TABLE I

Initial plasma properties, magnetic field strengths, and characteristic speeds at the equator and at the pole for the streamer and the flux-rope system.

	Pole		Equator	
	$1R_s$	$32R_s$	$1R_s$	$32R_s$
N_0 (cm^{-3})	10^8	3.8×10^2	10^8	3.78×10^2
T_0 (MK)	1.4	0.77	1.4	0.768
B_0 (gauss)	2.8	6.4×10^{-4}	1.14	5.62×10^{-4}
β_0	0.12	5	0.74	6.36
V_A ($km\,s^{-1}$)	609	72	249	63.1
V_{sw} ($km\,s^{-1}$)	3.58	360	0	323
C_f ($km\,s^{-1}$)	609	80	270	80
C_s ($km\,s^{-1}$)	108	72	28	63

N_0: number density (cm^{-3}), T_0: temperature (MK), B_0: initial magnetic field strength (gauss), β_0: plasma beta ($16\pi N_0 k T_0 / B_0^2$), V_A: Alfvén speed ($km\,s^{-1}$), V_{sw}: solar wind speed ($km\,s^{-1}$), C_f: fast wave speed ($km\,s^{-1}$), and C_s: slow wave speed ($km\,s^{-1}$).

TABLE II

Initial mass and energies for the streamer and flux-rope system. The energy is computed based on a depth of $0.1R_s$.

	Energy (10^{30} erg)				Mass (10^{16} g)	Total energy (10^{30} erg)
	Magnetic	Thermal	Kinetic	Gravitational		
Streamer	3.66	0.77	0.60	3.42	0.52	8.45
Rope	2.0	0.27	0	1.55	0.17	3.81
Rope + streamer	5.66	1.04	0.60	4.97	0.69	12.26

because the flow is supersonic and super-Alfvénic. As usual, the reiterative divergence-clearing technique in each time-step (Ramshaw, 1983) is used to guarantee that the solenoidal condition of the magnetic field (i.e., $\nabla \cdot \vec{B} = 0$) is satisfied.

To initiate these numerical experiments for the three chosen surface perturbations, the following expressions are used as numerical procedures:

(i) magnetic flux injection into the flux-rope

$$B_\varphi^{n+1} = B_\varphi^{n+1}\left[1 + \delta_B\left(1 - \frac{r^*}{0.85 r_f}\right)\right],$$

(ii) draining of mass from the flux-rope,

$$\rho^{n+1} = \rho^n\left[1 + \delta_\rho\left(1 - \frac{r^*}{0.85 r_f}\right)\right],$$

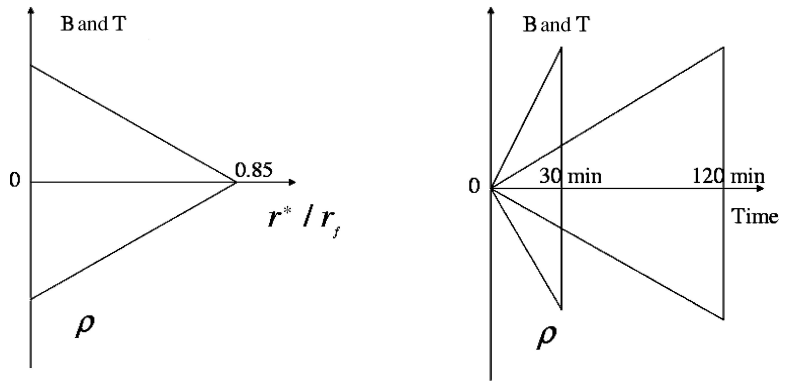

Figure 2. Schematic description of the spatial distribution (*left*) and the temporal distribution (*right*) of the perturbed quantities B, T, and ρ; r is the flux-rope radius, and r^* is the running variable in the radial direction.

(iii) heating the flux-rope

$$T^{n+1} = T^n \left[1 + \delta_T \left(1 - \frac{r^*}{0.85 r_{\rm f}}\right)\right],$$

where B_φ is the azimuthal component of the magnetic field, ρ the mass density, and T the temperature. r^* is the distance between the center of the flux-rope and the point where the strength of B_φ is raised; $r^* \leq 0.85\, r_f$ for this study, where r_f is the radius of the flux-rope, $\delta_{B,\rho,T}$ is an arbitrary constant related to the magnitude of the increasing (decreasing) field strength, mass or temperature. Finally, the superscript "n" indicates the time-step. The schematic descriptions for these three perturbed quantities as spatial and temporal profiles are given in Figure 2. It is worth noting that all these perturbations can be related to observations which we will discuss later. The numerical results corresponding to these perturbations are presented in the next section.

3. Numerical Results

A total of 12 cases of numerical experiments have been performed using the three basic types of perturbations; viz. injection of magnetic flux, draining the plasma from the flux rope and heating of the flux-rope, either employing only one type of perturbation or two or a combination of all three types. Table III shows the experiments carried out with these various perturbations, as well as the corresponding energy inputs.

Figure 3 shows the curves that portray the radial speed–time profiles (3a); the speed–distance profile (3b); and the distance–time profile (3c) for the 12 cases listed in Table III. To construct those curves, we have identified the CME front by

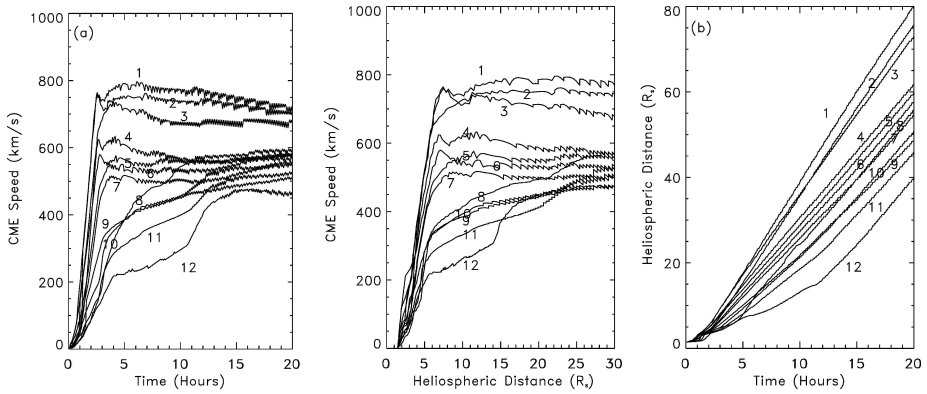

Figure 3. Simulation of (a) CME speed vs. time (b) CME speed vs. distance; and (c) CME distance vs. time, for the 12 cases of the numerical experiments shown in Table III.

choosing the location of maximum density in front of the flux-rope. Note that the wiggles present in all these curves are due to the numerical variation in locating the front of the CME within the grid. We have checked the relative errors between the grids and found them to be less than 1%.

These results clearly indicate that the profiles can be classified as belonging to two distinct groups; fast (constant speed) CMEs, and slow (gradual acceleration) CMEs as observed by MacQueen and Fisher (1983) and Andrews and Howard (2000). To obtain these results, the perturbations (δ_B, δ_ρ, and δ_T) were applied for a period of 120 min, with spatial and temporal variations as shown schematically in Figure 2. The amplitudes of these three perturbations are scaled by δ_B, δ_ρ, and δ_T, respectively. Quantitatively, the values $\delta_B = 0.004$ and $\delta_B = 0.008$ correspond to injected magnetic fluxes of 10^{21} Mx and 10^{22} Mx, respectively. These values are of the same order of magnitude as those observed by Wang *et al*. (2002). Similarly, $\delta_\rho = 0.004$ (0.008) means that the amount of mass being drained is 2% (5%) of the initial mass in the flux-rope; and $\delta_T = 0.004$ (0.008) corresponds to a temperature rise of a factor of 6 (36) from the initial state. The corresponding total energy inputs are given in Table III. These energy inputs are in the range between $\sim$1.5% and $\sim$30% of the initial state (Tables II and III). The maximum radial velocity, asymptotic radial velocity, and average acceleration during the eruptive phase are given in Table IV for these 12 numerical experiments. In the following, we will examine these 12 cases in detail.

3.1. Cases with single perturbation

Now, we examine in detail those cases with a single type of perturbation to understand how the surface perturbation affects the CME acceleration. Cases 8, 9,

TABLE III

Physical characteristics of the perturbations and their corresponding energy contents for all 12 cases of the numerical experiments.

Case	δ_B	δ_ρ	δ_T	Magnetic energy (erg)	Gravitational energy (erg)	Thermal energy (erg)	Total energy input (erg)
1	0.008	0	0.008	2.8×10^{30}	0	1.2×10^{30}	4×10^{30}
2	0	0	0.008	0	0	1.2×10^{30}	1.2×10^{30}
3	0.008	−0.008	0.008	2.8×10^{30}	2.2×10^{29}	8×10^{29}	3.8×10^{30}
4	0.008	−0.004	0	2.8×10^{30}	1.9×10^{29}	0	3×10^{30}
5	0.008	0	0	2.8×10^{30}	0	0	2.8×10^{30}
6	0.004	−0.004	0.004	8×10^{28}	1.9×10^{29}	1.4×10^{29}	4.1×10^{29}
7	0.004	−0.004	0	8×10^{28}	1.9×10^{29}	0	2.7×10^{29}
8	0	0	0.004	0	0	2×10^{29}	2×10^{29}
9	0.004	0	0	8×10^{28}	0	0	8×10^{28}
10	0	−0.004	0.008	0	1.9×10^{29}	8×10^{29}	1×10^{30}
11	0	−0.004	0.004	0	1.9×10^{29}	1.4×10^{29}	3.3×10^{29}
12	0	−0.004	0	0	1.9×10^{29}	0	1.9×10^{29}

TABLE IV

Eruption speeds, asymptotic speeds and average accelerations for the 12 cases of the numerical experiments.

Case	Max. eruption speed at 180 min ($km\,s^{-1}$)	Asymptotic speed ($km\,s^{-1}$)	Average acceleration at eruptive phase (<180 min) ($m\,s^{-2}$)
1	770	720	98
2	650	700	90
3	760	680	97
4	620	600	78
5	580	570	73
6	480	520	61
7	460	510	59
8	165	600	22
9	350	510	30
10	200	580	26
11	175	530	23
12	120	460	15

and 12 show that the amplitude of the perturbations are numerically the same (i.e., $\delta_T = 0.004$, $\delta_B = 0.004$, and $\delta_\rho = -0.004$). However, the amounts of energy input to the system corresponding to these perturbations as shown in Table III are quite different because of the nature of the perturbations. These differences in energy lead to different average accelerations and to different asymptotic speeds as shown in Table IV. These three cases exhibit characteristics of slow CMEs with gradual acceleration, as represented by curves 8, 9, and 12 shown in Figure 3. Note that case 12 shows a three-stage acceleration and deceleration process which may be due to the interaction between the magnetic buoyancy force and the ambient solar wind. We will return to this point later. In Cases 2 and 5, we increase the amplitude of the perturbations by a factor of 2 (i.e., $\delta_B = \delta_T = 0.008$). The velocity–time and velocity–distance profiles for these two cases, shown in Figure 3, indicate that these two cases definitely exhibit the characteristics of fast CMEs. Both of these cases show high radial speed and average acceleration during the eruptive phase (Table III). However, in the case of $\delta_\rho = -0.008$ (not shown), the whole structure collapsed after a short run of the numerical code. This behavior may have a physical cause; that is, if we drain too much mass from the flux-rope without providing additional support, the imbalance between the initial streamer and flux-rope will cause the collapse. On the other hand, if the additional perturbations of magnetic flux injection and heating are included, the streamer and flux-rope system will erupt to launch a CME, see for example Case 3.

In Cases 2 and 8, we compare thermal perturbations with different amplitudes (i.e., $\delta_T = 0.008$ and 0.004) and find that the higher the amplitude, the higher is the energy input, see Table III. As a consequence, different types of CMEs are produced (i.e., constant speed vs. gradually accelerated CMEs).

Now let us look at Cases 2 and 5. Even though the amount of energy resulting from the thermal perturbation (1.2×10^{30} erg) is smaller than the energy from the magnetic flux perturbation (2.8×10^{30} erg), the thermal pulse produces the higher asymptotic radial speed of the CME. This seeming anomaly may be understood by examining the dynamics of the evolution. The major force to propel the CME is the radial component of the Lorentz force. To estimate the magnetic energy input, the total magnetic field including all three components of the magnetic field is considered. This implies that only a fraction of the magnetic energy will convert to the radial component of the Lorentz force. On the other hand, the plasma pressure is isotropic, and most of the thermal energy can convert to the radial component of the pressure force. This is an indication that an active-region CME can produce a fast (constant speed) CME, as suggested by observations (Švestka, 2000).

In order to illustrate the magnetic buoyancy effect and the three stages of acceleration and deceleration of the CME shown in Figure 3 (curve 12, with flux-rope mass drainage only), we have plotted the evolution of the magnetic field at various times in Figure 4. We will later compare this evolution with the undisturbed radial velocity profiles of the solar wind and its characteristic fast- and slow-mode MHD wave speeds, C_f and C_s, shown in Figure 5. The characteristic speeds given here

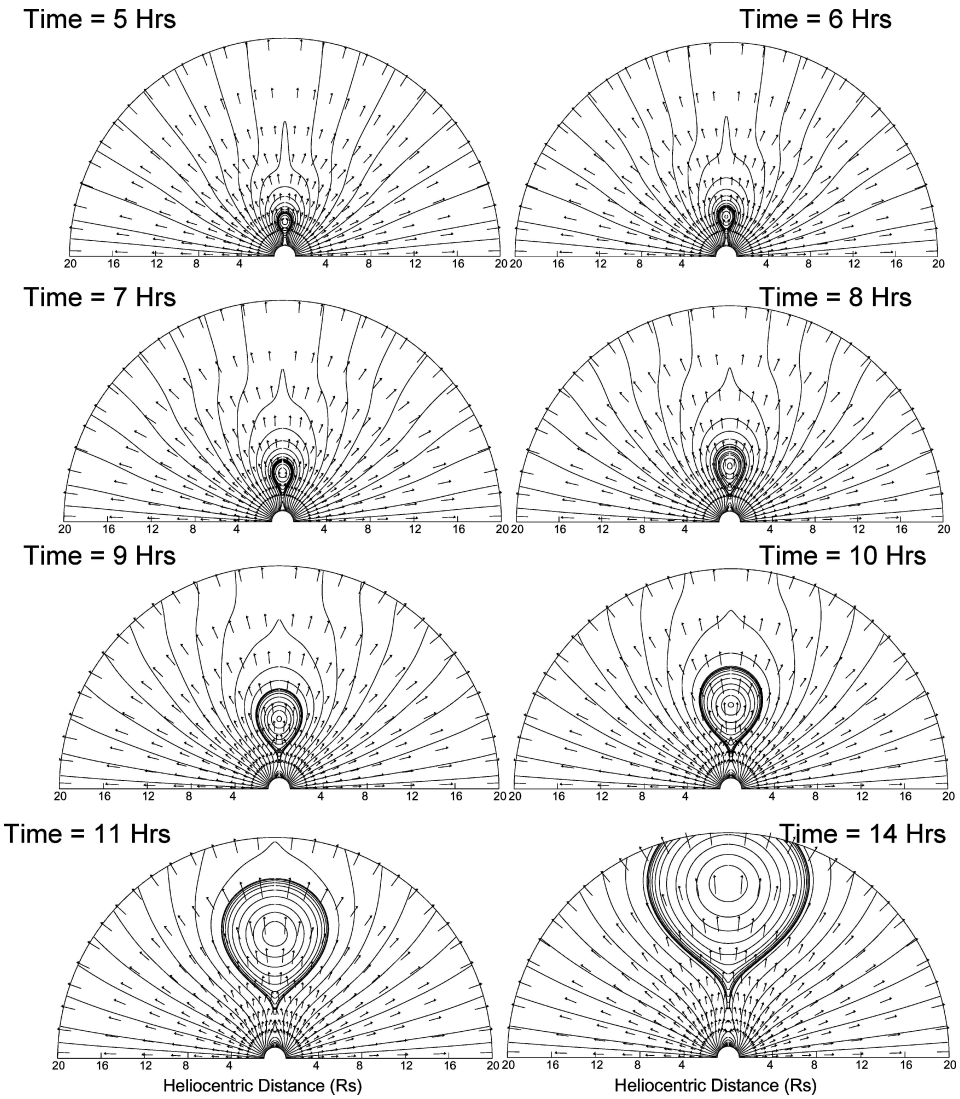

Figure 4. Evolution of magnetic field lines and of velocity vectors for Case 12 (plasma draining) at later time (5–14 hr).

will be used to locate the fast- and slow-mode MHD shocks later (Figure 9). Curve 12 of Figure 3 clearly indicates that the velocity of this CME is small ($\sim$20 km s^{-1}) at first, then after 1.5 hr it increases to $\sim$60 km s^{-1}. After 5 hr, when the CME has reached $\sim 6R_s$, the radial speed is $\sim$200 km s^{-1}. However, the solar wind speed at this location is $\sim$90 km s^{-1}, which is much less than the radial speed of the CME, and deceleration sets in (see Figure 3). Then, at $15R_s$, the ambient solar wind speed is $\sim$250 km s^{-1} (Figure 5), while the CME speed is less than

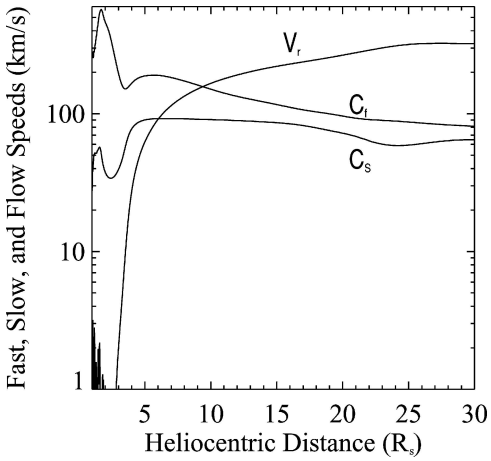

Figure 5. Initial radial distribution of the radial solar wind speed (V_r), MHD fast-mode wave speed (C_f) and MHD slow-mode wave speed (C_s).

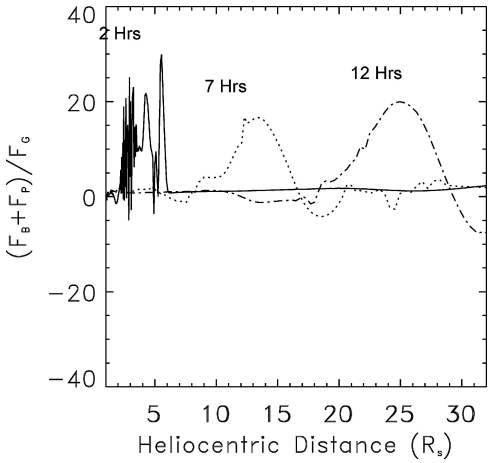

Figure 6. Radial distribution of the ratio of the magnetic force and the thermal pressure force to the gravitational force for Case 12 (plasma draining) at times 2, 7, and 12 hr.

the ambient solar wind speed, the CME gains momentum from the solar wind, and it begins to accelerate again. We also notice from the evolution of the magnetic field topology shown in Figure 4, that there is an accelerated expansion between the 11th and 14th hour due to the renewed magnetic buoyancy force (indicated at $t = 12$ hr) shown in Figure 6. Since we have identified the CME front as the density peak in front of the leading edge of the flux rope, this is another ingredient to accelerate the CME. When the CME speed again exceeds the solar wind speed, the CME will again show a deceleration. Through these interactions, the CME will finally attain its asymptotic speed of $\sim$460 km s^{-1} as shown in Table IV for this

case. A closer inspection of Figure 4 reveals further details of the acceleration process. When the flux-rope moves upward, a current sheet is formed at the trailing edge of the flux-rope, and this current sheet will develop a force to hold down the flux-rope. However, Figure 4 shows that around 11 hr magnetic reconnection sets in, freeing the flux-rope from the confining force. As a result additional acceleration occurs, as shown in Figure 3. This phenomenon also explains why the initial acceleration is so slow, being constrained by the confining force in the magnetic configuration of inverse type prominences as suggested by Low and Zhang (2002).

Let us examine Case 12 for further insight of how the buoyancy force works in the CME evolution process. We have plotted at different times (i.e., 2, 7, and 12 hr) in Figure 6 the ratio between the upward force (i.e., radial component of the Lorentz force and the pressure gradient) and the downward gravitational force. The draining of mass from the flux-rope will decrease the downward gravitational force, thus creating the upward buoyancy as indicated by the ratio of the forces shown in Figure 6. The ratio $(F_B + F_P/F_G)$ increases as F_G decreases. Further, F_P will also decrease, that is, since the pressure force is calculated from $p = \rho RT$, and the temperature is changed very little in the present model when the mass is drained, the F_P will decrease. In this case, we have not injected new magnetic flux into the flux-rope; hence, the Lorentz force variation is based on the initial state, where the field decreases along the radial direction. We suggest that the combined observed increase of this ratio (as time increased) shown in Figure 6, is the indication of the buoyancy action.

Let us look further at the single-pulse Cases 2 and 8, and the Cases 5 and 9. These are cases of temperature and magnetic flux perturbations with a difference of a factor of 2 of the perturbed parameters (δ_T and δ_B). Cases 2 and 8 result from a temperature perturbation, respectively of 36 and 6 times the initial temperature (1.2×10^6 K). These two pulses produce a thermal energy input to the flux rope of 1.2×10^{30} erg and 2×10^{29} erg, respectively. The amount of energy input for Case 2 is six times higher than for Case 8. Because of the increase of the energy into the flux rope, the velocity profiles show dramatic differences, as shown in Figure 3. The larger energy input (Case 2) produces a fast CME, and Case 8, with a factor of six less energy input, produces a slow CME. Similar behaviors are also shown for Case 5 and Case 9. These results show that the amount of energy input has a significant effect.

3.2. Cases with combined perturbations

We now turn our attention to those cases in which all three perturbations have been combined. In Cases 3 and 6 the nature of the pulses is the same (δ_B, δ_ρ, and δ_T), i.e., they have similar acceleration processes, but the amplitudes of the accelerations are different. In both cases fast CMEs are produced, but with different magnitudes of

the asymptotic radial velocity at $30R_s$. As expected, the higher energy input gives the higher radial velocity as shown in Table IV. However, this is not always true as discussed in Section 4.

In Cases 4 and 7 we study the effect of two combined pulses, δ_B and δ_ρ. The amplitude of δ_ρ is kept the same in both cases, but the amplitude of δ_B is twice as big in Case 4 as in Case 7. The resulting velocity profiles shown in Figure 3 classify both ejections as fast CMEs. The profiles exhibit a similar behavior, but also show that the larger the δ_B input, the larger the resulting radial velocity. Case 10 and Case 11 are performed by combining the two pulses, δ_ρ and δ_T. We have kept δ_ρ constant but changed δ_T for these two cases. The results shown in Figure 3 indicate that both cases lead to slow CMEs with different final propagation velocities.

As noted, the energy input for Case 3 includes all three types of perturbations (i.e., $\delta_B = \delta_T = 0.008$ and $\delta_\rho = -0.008$), and results in a constant-speed, fast CME as shown in Curve 3 of Figure 3. This particular CME reaches a radial speed of 760 km s^{-1} during the eruptive phase and then attains an asymptotic speed of 680 km s^{-1}. The deceleration is caused by the slow background solar wind speed (see Figure 5). The average acceleration reaches 97 km s^{-2} for this case. In Case 1, the perturbation includes δ_B and $\delta_T = 0.008$ without any mass draining, and this gives the highest speed and acceleration found in the study. One might expect that Case 3 would have had the highest velocity and acceleration because all three driving mechanisms are involved. The reason why Case 3 did not match Case 1, even though the amount of energy input is about the same, is due to the fact that, when the mass is drained, the pressure force is accordingly reduced. This interplay of forces implies that the gain from magnetic buoyancy cannot compensate for the loss in the pressure force.

The duration of the pulses is 120 min in all cases discussed above. In order to understand the effect on CME acceleration of the duration of the applied pulses, we have carried out additional numerical experiments for 30 min pulses, again with various amplitudes and corresponding total energy inputs, as shown in Table V. From these results (i.e., radial speed vs. time and heliocentric distance) shown in

TABLE V

The energy contents of the perturbations used to obtain the results shown in Figure 7 for a pulse duration of 30 min.

Case	δ_B	δ_ρ	δ_T	Magnetic energy (erg)	Gravitational energy (erg)	Thermal energy (erg)	Total energy input (erg)
1	0.04	−0.008	0.04	5.4×10^{30}	12.2×10^{29}	1.7×10^{30}	7.3×10^{30}
2	0.025	−0.008	0.025	3×10^{29}	2.2×10^{29}	4×10^{29}	9.2×10^{29}
3	0.015	−0.008	0.015	4.2×10^{29}	2.2×10^{29}	1.5×10^{29}	4.1×10^{29}

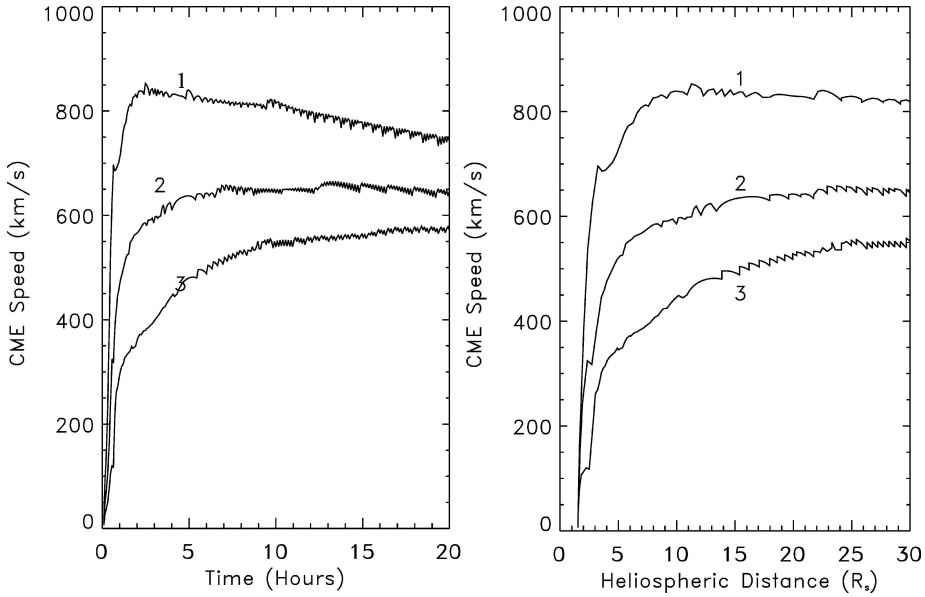

Figure 7. The CME speed vs. time (*left*) and CME speed vs. distance (*right*) for a short-duration (30 min) pulse with three different amplitudes: (1) $\delta_B = 0.04$, $\delta_\rho = -0.008$ and $\delta_T = 0.04$; (2) $\delta_B = 0.025$, $\delta_\rho = -0.008$ and $\delta_T = 0.025$; and (3) $\delta_B = 0.015$, $\delta_\rho = -0.008$ and $\delta_T = 0.015$. The corresponding amounts of energy resulting from these pulses are shown in Table V.

Figure 7, we recognize, once again, that the higher rates of energy inputs produce explosive, fast CMEs (i.e., higher constant speed CMEs). Otherwise, slow CMEs result. If we increase the input further, the CME propagation speed may reach $\sim$1500 km s^{-1}, as shown in Figure 8.

Finally, we plot the location of the MHD fast shock as a function of the average acceleration as shown in Table IV for the originally discussed 12 cases portrayed in Figure 9. This plot clearly illustrates that the location of the CME-induced MHD fast shock (as its initial formation) depends on the magnitude of the CME acceleration. The development of an MHD fast shock will be inversely proportional (i.e., will develop closer to the Sun) to the magnitude of the CME's acceleration. Note that the location of the MHD fast shock is defined as the place where the ratio of the local flow speed to the fast-mode MHD wave speed becomes larger than the unity. No slow shocks were found in this study.

4. Concluding Remarks

We have conducted a series of numerical experiments to investigate the acceleration processes of CMEs. A streamer and flux-rope model (Wu and Guo, 1997) was used with consideration of three basic driving mechanisms, viz. (i) injection of magnetic

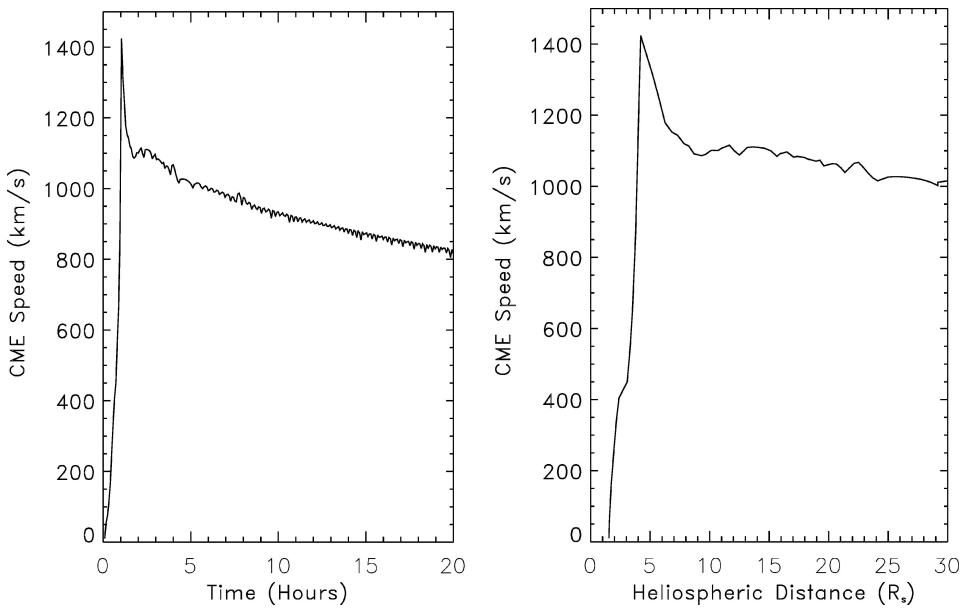

Figure 8. The CME speed vs. time (*left*) and CME speed vs. distance (*right*) for a pulse of one-hour duration and with amplitude $\delta_B = 0.025$, $\delta_\rho = -0.004$ and $\delta_T = 0.025$. The amplitude of this pulse is similar to the pulse creating curve 2 in Figure 7, except that a factor of 2 less plasma is drained. The pulse produces a very fast CME. When plasma is less drained and the pressure also reduces to the level below that for the case of curve 2 (Figure 7). Thus this pulse produces a very fast CME.

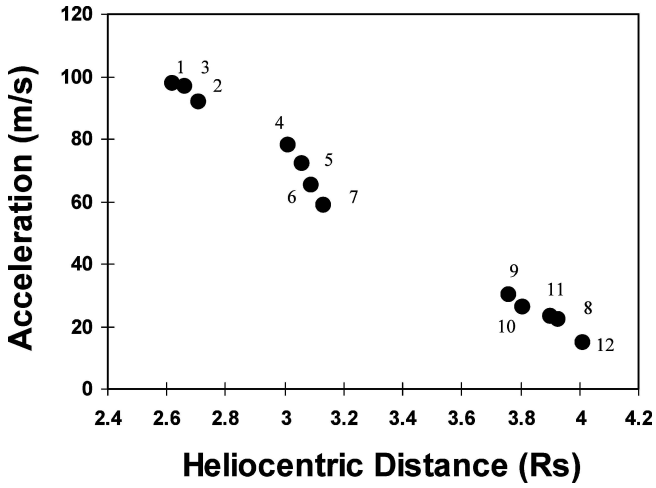

Figure 9. The MHD fast-shock location as a function of the magnitude of the CME acceleration and distance from the solar surface, where numerical numbers indicate the case number as listed in Tables III and IV.

flux into the flux-rope, causing an additional Lorentz force to launch a CME; (ii) draining of plasma from the flux-rope, triggering a magnetic buoyancy force which causes the flux-rope to lift up and launch a CME; and (iii) introducing additional heating by raising the temperature of the flux-rope to mimic an active-region flux-rope accompanied by a flare to launch a CME. Using these three fundamental perturbations, we have studied 12 cases of CME acceleration and deceleration, either using a single perturbation or various combinations thereof. Briefly stated, the total energy inputs from the perturbations determine the speed of the resulting CMEs and their acceleration in such a way that the higher the perturbation energy input, the faster is the created CME, as shown in Tables III and IV. However, there are a few exceptions, viz. Cases 2 and 3, where the higher energy input did not produce a faster CME. The reason for this is that the pressure force is decreased for those cases because of drainage of mass.

Now let us examine Case 9 vs. Case 12; Case 9 vs. Case 10; and Case 2 vs. Case 5. These cases again show that the higher energy inputs do not, necessarily, produce the higher CME speeds. To understand the physical reason for this behavior, we have plotted in Figure 10 the variation of the ratio of the total forces applied in three cases, e.g., F_9/F_{12}, F_9/F_{10}, F_2/F_5 as a function of heliocentric distance, and at a time 2 hr after initiation. From these results, we recognize that these ratio are not always greater than unity. Thus, these results imply that a higher energy input does not always produce a stronger force to propel the CME. This situation indicates that it is the conversion from energy to momentum that is critical in the CME acceleration process. By looking at Table III and Figure 3, we note that heating is the most efficient process to convert energy into momentum; next in efficiency is magnetic flux injection, and least efficient is plasma draining from the flux-rope. This may be understood in terms of the nature of the perturbations. Heating will produce a pressure increase which leads most directly to conversion of energy to momentum; magnetic flux injection produces an additional Lorentz force, but only the produced radial Lorentz force is available for CME acceleration. Finally, plasma draining triggers magnetic buoyancy, which is a slow dynamic process for overcoming gravitational energy such that the former can provide a radial force for CME acceleration. The above argument explains why an active-region CME (often flare-associated) is always a fast CME (Švestka, 2000).

We have also studied the effect of different rates of inputs and find that the higher rates (Figures 7 and 8) produce more explosive CMEs. For example, the CME speed reaches $\sim$1500 km s^{-1} within an hour, as shown in Figure 8, and the MHD fast shock appears within $3R_s$. Finally, the present simulation shows that the acceleration occurs in the region from $\sim 1.5R_s$ to $\sim 15R_s$ while the data given by MacQueen and Fisher (1983) have an acceleration region between $1.25R_s$ and $2.4R_s$. This discrepancy is due to the fact that the present simulation configuration has a global magnetic dipole streamer which covers the whole Sun. If we scale properly by using a local geometric configuration such as a 30° bi-polar configuration with

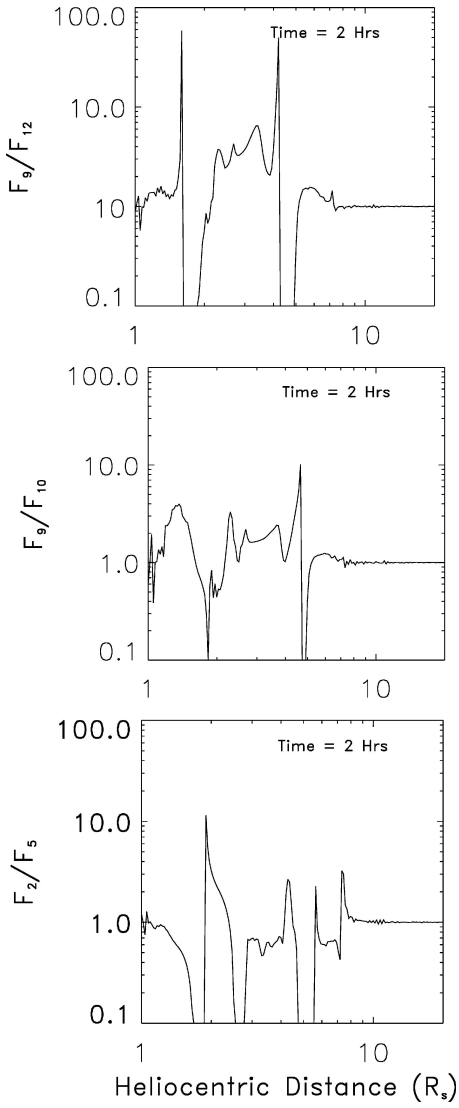

Figure 10. The ratio of the total forces at the equator in logarithmic scale applied in Case 9 vs. Case 12; Cases 9 vs. Case 10; and Case 2 vs. Case 5 at 2 hr after initiation. Note the heating (Case 2, *lowest panel*) has some of the lower relative forces but achieves some of the highest CME speeds (Figure 3) despite the fact that the magnetic influx (Case 5) has a higher energy input (Table III). Similarly, Case 9 (magnetic flux, *top panel*) has higher forces, but lower energies than Case 10 and 12 and higher CME speeds.

the proper choice for the flux-rope size, which is 1/6 of the present size, then the simulation would refer to the region 1 to $2.5R_s$. The basic simulated characteristics would be qualitatively similar, and the MHD shock would develop close to the Sun as shown in Figure 9.

We briefly summarize some important findings of the present numerical simulation experiments as follows:

1. The inverse-type prominence magnetic field configuration has the ability to produce kinematic properties of both fast (constant speed) and slow (gradually accelerated) CMEs, depending on the surface conditions.
2. From the 12 cases of simulation experiments, we notice that if the perturbation energy is larger than ∼24% of the initial energy of the structure (streamer and flux-rope), a fast CME will result (i.e., a CME with velocity higher than 600 km s^{-1}, the escape velocity) as shown in Figure 3, Tables II, III, and IV.
3. A large energy input is a necessary condition to produce a fast CME, but it is not sufficient. The nature of the perturbation will play an important role (Tables III and IV).
4. The present numerical simulation experiments qualitatively reproduce the observations given by *Skylab* data (MacQueen and Fisher, 1983) and SOHO/LASCO data (Andrews and Howard, 2000).
5. The ambient solar wind plays an important role to affect the acceleration and deceleration of the CMEs.
6. To our knowledge, this is the first numerical simulation to test plasma draining from a flux-rope to trigger magnetic buoyancy and propel a CME above the observed erupting filament (flux-rope) (Tandberg-Hanssen, 1995).

There remains the important question of what will happen if we consider a normal-type prominence magnetic configuration, instead of the inverse-type studied in this paper. Magnetic reconnection may play a somewhat different role, a question that will be the focus of a future study.

Acknowledgements

The authors would like to thank Dr Murray Dryer for reading the manuscript and providing many valuable suggestions. The work performed by STW and TXZ is supported by NASA Grant NAG5-12843, NSF grant ATM 0316115 and Subcontract with AAMU-NNG04GD59G; Y. Liu is supported by NASA grant NAG5-13261, Feng X.S. is supported by NSF, China (4037405, 40204010, 40336053) and the one-hundredth talent program of the CAS (49925412, 40141055), and A. Tan is supported by NASA Grant NNG04GD59G.

References

Amari, T. J., Luciani, F., Mikić, Z., and Linker, J.: 2000, *Astrophys. J.* **529**, L49.
Andrews, M. D. and Howard, R. A.: 2000, *Space Sci. Rev.* **95**, 147.
Antiochos, S. K., DeVore, C. R., and Klumchuk, J. A.: 1999, *Astrophys. J.* **510**, 485.
Chen, J. and Krall, J.: 2003, *J. Geophys. Res.*, **108**, A11, 1410.

Chen, J. R., Howard, A. Brueckner, G. E., Santoro, R., Krall, J., Paswaters, S. E., St. Cyr, O. C., Schwenn, R., Lamy, P., and Simnett, G. M.: 1997, *Astrophys. J.* **490**, L 191.
Gosling, J. T., Hildner, E., MacQueen, R. M., Muroe, R. H., Poland, A. I., and Ross, C. L.: 1976, *Solar Phys.* **48**, 389.
Guo, W. P., Wu, S. T., and Tandberg-Hanssen, E.: 1996, *Astrophys. J.* **469**, 944.
Liu, W., Zhao, X. P., Wu, S. T., and Scherrer, P. H.: 2003, Proc. ISCS 2003 Symposium, Solar Variability as an Input to the Earth's Environment, *ESA SP* **535**, 459.
Low, B. C.: 1990, *Ann Rev. Astron. Astrophys.* **28**, 491.
Low, B. C. and Zhang, M.: 2002, *Astrophys. J.* **564**, L53.
MacQueen, R. M. and Fisher, R. R.: 1983, *Solar Phys.* **89**, 89.
Plunkett, S. P., Vourlidas, A., Šimberová, S., Karlický, J., Kotrč, P., Heinzel, P., Kupryakov, Y. A., Guo, W. P., and Wu, S. T.: 2000, *Solar Phys.*. **194**, 371.
Ramshaw, J.D.: 1983, *J. Comput. Phys.* **52**, 592.
Shafranov, V. D.: 1960, *Soviet Phys. JETP* **37**, 775.
Sheeley, N. R. Jr., Walters, J. H., Wang, Y.-M., and Howard, R. A.: 1999, *J. Geophys. Res.* **104**, 24739.
St. Cyr, O. C., Burkepile, J. T., Hundhausen, A. J., and Lecinski, A. R.: 1999, *J. Geophys. Res.* **104**, 12493.
St. Cyr, O. C. *et al.*: 2000, *J. Geophys. Res.*, **105**, 18169.
Švestka, Z.: 2000, *Space Sci. Rev.* **95**, 135.
Tandberg-Hanssen, E.: 1995, *The Nature of Solar Prominence*, Kluwer, Dordrecht.
Tousey, R.: 1973, *Adv. Space Res.* **13**, 713.
Wang, H. M., Spirock, T. J., Qiu, J., Ji, H. S., Yurchyshyn, V., Moon, Y.-J., Denker, C., and Goode, P. R.: 2002, *Astrophys. J.* **576**, 497.
Wu, S. T. and Wang, J. F.: 1987, *Comp. Method Appl. Mech. Eng.* **64**, 267.
Wu, S. T., Guo, W. P., and Wang, J. F.: 1995, *Solar Phys.* **157**, 325.
Wu, S. T., Guo, W. P., and Dryer, M.: 1997, *Solar Phys.* **170**, 265.
Wu, S. T., Guo, W. P., *et al.*: 1997, *Solar Phys.* **175**, 719.
Wu, S. T., Guo, W. P. Burlaga, L. F., and Michels, D.: 1999, *J. Geophys. Res.* **104**, A7, 14,789.
Wu, S. T., Guo, W. P., Plunkett, S. P. Schmieder, B., and Simnett, G. M.: 2000, *J. Atmos. Solar-Terr. Phys.* **62**, 1489.
Zhang, M., Golub, L., DeLuca, E., and Burkepile, J.: 2002, *Astrophys. J.* **574**, L97.